Journal of Ceramic Processing Research. Vol. 17, No. 7, pp. 742~746 (2016)

J O U R N A L O F
Ceramic Processing Research

Effects of phase additions on three dimensionally ordered macroporous structure of SiO_2-CaO-P_2O_5 bioactive glasses

Thanida Charoensuk[a], Chitnarong Sirisathitkul[a,*], Upsorn Boonyang[a], Innocent J. Macha[b], Yaowarat Sirisathitkul[c] and Besim Ben-Nissan[b]

[a]*Molecular Technology Research Unit, School of Science, Walailak University, Nakhon Si Thammarat, Thailand*
[b]*Department of Chemistry and Forensic Science, University of Technology Sydney, Australia*
[c]*School of Informatics, Walailak University, Nakhon Si Thammarat, Thailand*

The three-phase of SiO_2-CaO-P_2O_5 bioactive glass was successfully fabricated with three dimensionally ordered macroporous (3DOM) structure by incorporating a colloidal crystal template in the sol-gel synthesis. Whereas the composition and purification of all four- and five-phase bioactive glasses were obtained after the inclusion of sodium nitrate and ferric nitrate nonahydrate, the phase additions resulted in the deformation of the scaffolds and the curved walls were thinner with larger variations in size. Such difference was due to the gel-coating on spherical crystals instead of the filling in the interstitial holes of the template. Moreover, the bioactive glass microspheres were formed on the surface of the scaffolds due to the strong precursor-template interactions. Nevertheless, the five-phase bioactive glasses exhibited the thermal stability up to 1000 ºC with slight mass loss and heat transfer.

Key words: Bioactive glass, Sol-gel method, Macropore, Iron oxide, Thermal properties.

Introduction

Three dimensionally ordered macroporous (3DOM) bioactive glasses possess considerable advantages in bone and tissue regenerations [1, 2]. To enhance their properties and functions, additional ions or compound phases are incorporated in conventional three-phase SiO_2-CaO-P_2O_5 glass. For examples, the addition of Na_2O promotes the ion exchanges in bioactivity [3]. The metabolic activity in osteoblast proliferation can be improved by Sr in bioactive glasses [4, 5]. The doped Li increases antibacterial properties [6] whereas the incorporation of C enhances compressive strength [7]. Furthermore, the magnetic phase sensitive to the external field is useful for bioactive glasses in local drug delivery and hyperthermia treatments [8-10].

Owing to its versatility and facility, the sol-gel process has widely been implemented in the research and development of nanoporous glasses and ceramics [3, 10-12]. The bioactivity and biodegradability could be enhanced via hierarchical porous scaffolds [3]. Whilst it has the great benefit to develop the multifunctional bioactive glass, the practical application is complicated due to several chemical interactions. The effects during the sol-gel process are manifested in the bioactive glass products with varying properties. For an example, chemical interaction involving MgO modified structure of porous bioactive glasses [12]. However, the reports so far on 3DOM bioactive glasses are lacking.

Three-, four- and five- phase bioactive glasses were compared in this study. The effects of phase additions on the 3DOM structure and thermal stability of bioactive glass scaffolds were demonstrated.

Experimental

In the one-pot sol-gel synthesis with acidic catalyst, the three-phase SiO_2-CaO-P_2O_5 bioactive glass was synthesized by tetraethyl orthosilicate (TEOS, $C_8H_{20}O_4Si$), calcium nitrate tetrahydrate (CNT, $Ca(NO_3)_2 \cdot 4H_2O$) and triethyl phosphate (TEP, $C_6H_{15}O_4P$). Whereas the mesoporous structure was generated by triblock copolymer P123, hierarchical scaffolds with the macroporous structure were obtained from poly methyl methacrylate (PMMA) colloidal crystal template. Spherical PMMA with diameter of 325 nm were prepared following the method from the literature [13].

All processing steps were shown in forms of a diagram in Fig. 1 and chemicals used are summarized in Table 1. The chemical solutions were mixed and stirred until reaching the gel point. The gels were aged at 45 ºC for 24 hrs, dried at 45 ºC for 24 hrs and calcined at 600 ºC for 6 hrs to obtain final 3DOM bioactive glasses. The four-phase SiO_2-CaO-P_2O_5-Na_2O bioactive glass was synthesized by using a similar procedure with the addition of sodium nitrate ($NaNO_3$). Finally, five-phase magnetic bioactive glasses were prepared by further inclusion of ferric nitrate nonahydrate ($Fe(NO_3)_3 \cdot 9H_2O$) in starting

*Corresponding author:
Tel : +66-75-673-812
E-mail: chitnarong.siri@gmail.com

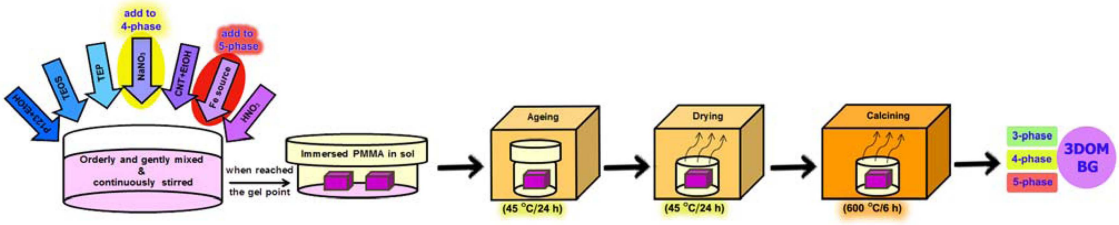


Fig. 1. Diagram of synthesis procedures for three-, four- and five-phase bioactive glasses.

Table 1. Chemicals used in the synthesis of three-, four-, and five-phase bioactive glasses.

Sample codes	Composition SiO_2-CaO-P_2O_5-Na_2O-Fe (mol %)	P123 (g)	TEOS (ml)	TEP (ml)	$NaNO_3$ (ml)	$Ca(NO_3)_2 \cdot 4H_2O$ (g)	$Fe(NO_3)_3 \cdot 9H_2O$ (g)	1M HNO_3 (ml)	EtOH (ml)
3 phase	80-15-5-0-0	0.667	1.79	0.15	–	0.354	–	1.00	2.50
4 phase 80S/0Fe	80-10-5-5-0	0.667	1.79	0.15	1.00	0.236	–	1.00	2.50
5 phase 70S/10Fe	70-10-5-5-10	0.581	1.57	0.15	1.00	0.236	0.404	1.00	2.50
60S/20Fe	60-10-5-5-20	0.506	1.34	0.15	1.00	0.236	0.808	1.00	2.50
50S/30Fe	50-10-5-5-30	0.417	1.12	0.15	1.00	0.236	1.212	1.00	2.50

materials with three varying compositions.

The obtained samples were characterized by field emission scanning electron microscopy (FE-SEM; Zeiss Merlin Compact) operated at 15 kV, energy dispersive spectrometry (EDS; Oxford Aztec) and X-ray diffractometry (XRD; D8 Advance Bruker) using Cu Ka radiation from 10 to 70 ° with a step of 0.02 °/min. Fast fourier transform infrared (FTIR; Bruker Tensor27) spectroscopy was carried out on KBr-bioactive glass pellets in the transmission mode with a mid-infrared range 400-4000 cm^{-1} at the resolution of 4 cm^{-1}. Thermal properties of five-phase bioactive glasses were characterized by simultaneous thermogravimetric analysis (TGA)-differential scanning calorimetry (DSC) (SDT Q600) using the heating rate of 10 ºC/min and the air flow rate of 30 ml/min.

Results and Discussion

Phase and structure

After removing PMMA templates by thermal treatment at 600 ºC, every obtained sample has glittering opal-like appearance due to the optical reflection from porous surface. For the three-phase bioactive glass in Fig. 2, vibrational peaks in FTIR spectra are assigned to the characteristic bonding of bioactive glass structures [3]. The peaks at 471 cm^{-1} (bending mode), 802 cm^{-1} (symmetric stretching mode), 1095 cm^{-1} and the shoulder at 1095-1220 cm^{-1} (asymmetric stretching mode) correspond to the vibration of Si-O-Si bonds. The peak at 567 cm^{-1} correlates to the P-O bending mode. In additions, the vibrational peaks at 1630 cm^{-1} (bending mode) and 3448 cm^{-1} (stretching mode) assigned to O-H bonds indicate residual water trapped inside the glass structure. For the carbonate group, the vibrational peaks around 1414 cm^{-1} and 1448 cm^{-1} are

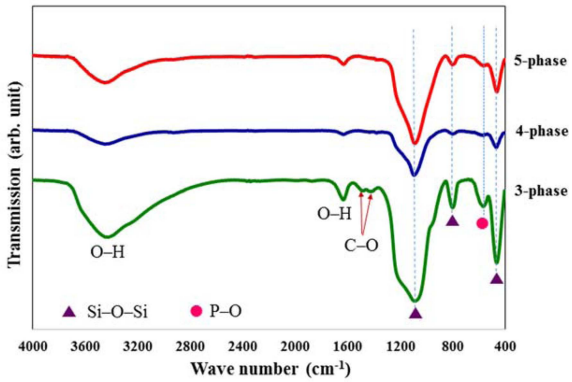


Fig. 2. FTIR spectra showing an identical chemical structure of three-, four- and five-phase (70S/10Fe) bioactive glasses.

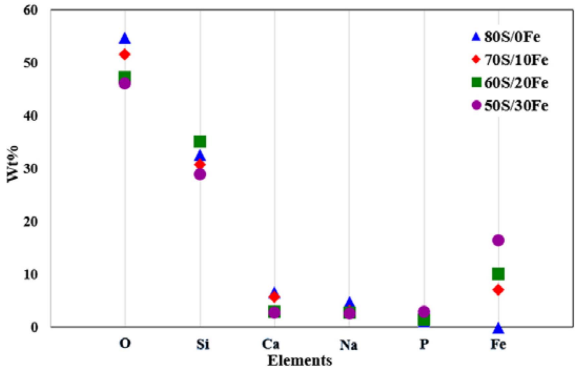


Fig. 3. Comparison of average elemental compositions of 4-phase (80S/0Fe) and five-phase (70S/10Fe, 60S/20Fe, 50S/30Fe) bioactive glasses by EDS.

assigned to the asymmetric stretching mode of C-O bond of CO_3^{2-} inherited from a carbonation process during the heat treatment. No additional peak is observed in the case of four- and five-phase bioactive glasses in Fig. 2. The

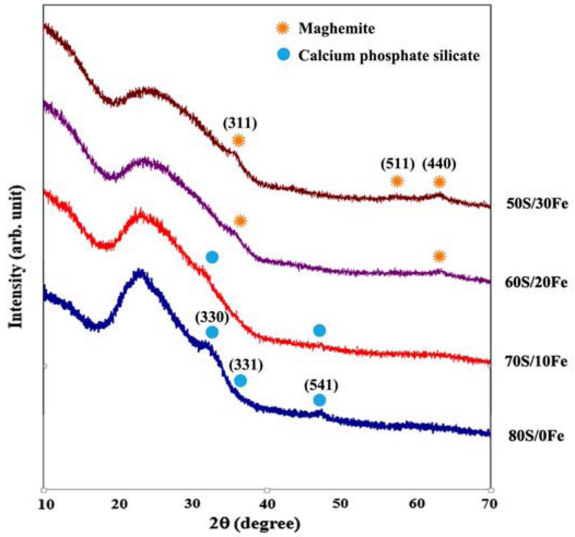


Fig. 4. XRD spectra of four-phase (80S/0Fe) and five-phase (70S/10Fe, 60S/20Fe, 50S/30Fe) bioactive glasses.

characteristic bands of bioactive glasses are retained and the addition of either 5% mol Na_2O or 10% mol Fe is not sufficient to make relevant vibrations observable in FTIR spectra.

The elemental compositions of the four-phase SiO_2-CaO-P_2O_5-Na_2O and five-phase bioactive glasses with three varying Fe proportions are averaged from EDS detection over 10 points on each sample and compared in Fig. 3. The composition of each element may be slightly different from those associated to precursors but agrees reasonably well with the ratio used and indicates no impurity like FTIR results. The EDS results also confirm the enhancement of Fe proportion in bioactive glasses by increasing ferric nitrate nonahydrate in the sol-gel synthesis. From XRD patterns in Fig. 4, broad diffraction peaks around 20-25 ° indicate the amorphous nature of glassy samples without any sharp peak at higher angles. Samples 80S/0Fe and 70S/10Fe exhibit observable peak at 31.7 °, 34.5 °, 48.4 ° respectively corresponding to (330), (331), and (541) planes of calcium phosphate silicate (JCPDS 040-0393). By increasing the proportion of Fe in the case of samples 60S/20Fe and 50S/30Fe, weak peaks at 35.6 °, 57.2 °, 62.7 ° are detected as a result of the diffraction from (311), (511), and (440) planes of γ-Fe_2O_3 (maghemite) nanocrystals (JCPDS 04-0755). During the thermal decomposition in these five-phase bioactive glasses, the reducing carbon from P123 may participate in iron oxide conversion [14].

Morphology

In Fig. 5(a), the FE-SEM image of three-phase bioactive glass reveals the 3DOM scaffolds inherited from the spherical PMMA colloidal crystal template. The ordered spacing indicates the inverse opal effect. Clearly, the sol penetrated into the octahedral and

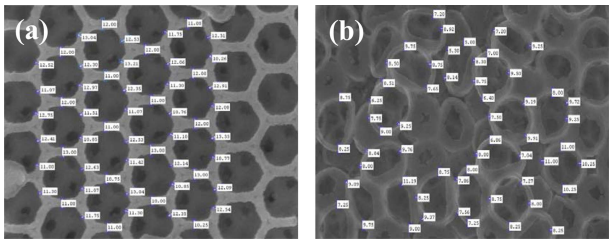


Fig. 5. FE-SEM micrographs of (a) three-phase and (b) four-phase bioactive glasses. The numbers indicate the relative graphic width which can be multiplied by the factor 5.4 to obtain the real width in nm.

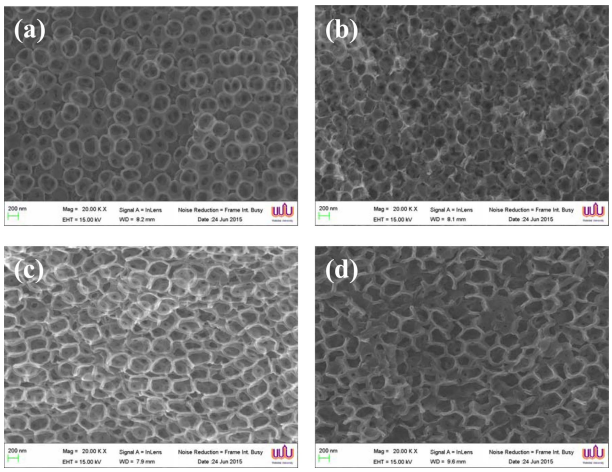


Fig. 6. FE-SEM micrographs of (a) four-phase and (b-d) five-phase (70S/10Fe, 60S/20Fe, 50S/30Fe) bioactive glasses.

tetrahedral holes of the *fcc* structural template forms gel and becomes the bioactive glass matrix by the calcination. The sol can completely fill the interstitial holes in this three-phase 3DOM bioactive glass. The resulting pores are orderly arranged and partitioned by skeleton walls with the width ranging from 54-72 nm.

The addition of Na_2O phase leads to the spherical surface coating of the four-phase bioactive glass by the sol. Fig. 5(b) reveals the tendency for spherical surface coating in contrast to complete fills in the interstitial holes of the *fcc* structure during the gel formation. Hence, the non-template void space and the hollow shapes in the interstitial region of the template are obtained with deviations from 3DOM morphology. The rounded pores have curved skeleton walls with a smaller average thickness of 45 nm and a larger standard deviation.

In Fig. 6, the scaffolds are increasingly distorted with the rise in Fe proportion in five-phase bioactive glasses. Moreover, the structure is partly collapsed in the case of sample 50S/30Fe. The metal salt additives tend to promote the gel phase. The molecular charge interactions occur between precursors and templates. The attractive and repulsive forces affect the surface coating and result in the phase separation of the excess chemicals [15].

Attention is also paid to microspheres formed on the

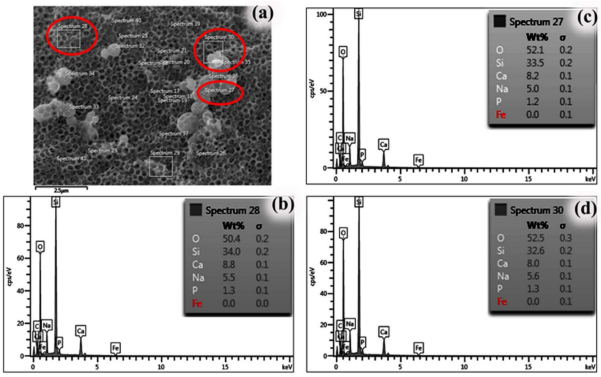


Fig. 7. (a) Microspheres on the surface of four-phase bioactive glass visualized by FE-SEM image and (b-d) EDS spectra indicate elemental compositions of SiO_2-CaO-Na_2O-P_2O_5 at three different positions.

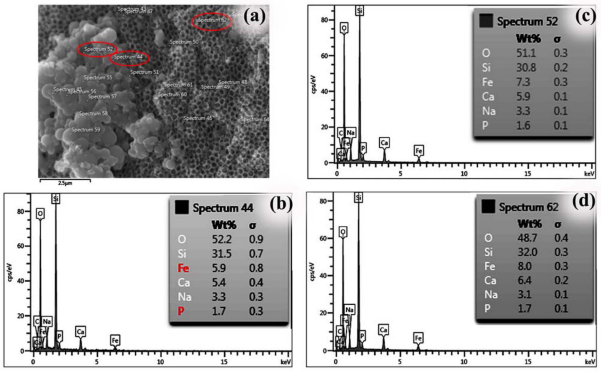


Fig. 8. (a) Microspheres on the surface of five-phase bioactive glass visualized by FE-SEM image and (b-d) EDS spectra indicate elemental compositions of SiO_2-CaO-Na_2O-P_2O_5 incorporating iron oxide at three different positions.

surface of four- and five-phase bioactive glasses, respectively exemplified in Figs. 7(a) and 8(a). The EDS spectra in Figs. 7(b-d) and 8(b-d) indicate the purity and comparable elemental composition in microspheres and pores. The phase separation is probably induced by the metal salt additives. The interactions between bioactive glass precursors and the additive molecules likely result in the increase of the gel phase. During the gelation process, the bioactive glass precursors coat the spherical surface of the template due to the strong precursor-template interactions. The excess precursors then move from the inside to outside and form microspherical bioactive glass mostly distributed over the external surface.

Thermal properties

Thermal properties of five-phase bioactive glasses are demonstrated by DSC, TGA and derivative thermogravimetric analysis (DTG) thermographs in Fig. 9. Every sample exhibits a slight TGA mass loss indicating their thermal stability. The calcination at 600 ºC for 6 hrs eliminates P123, PMMA templates as well as by-products and converts the dried gel to the glass phase. The increase in Fe from 10% to 30% at the expense of SiO_2 composition results in the successive

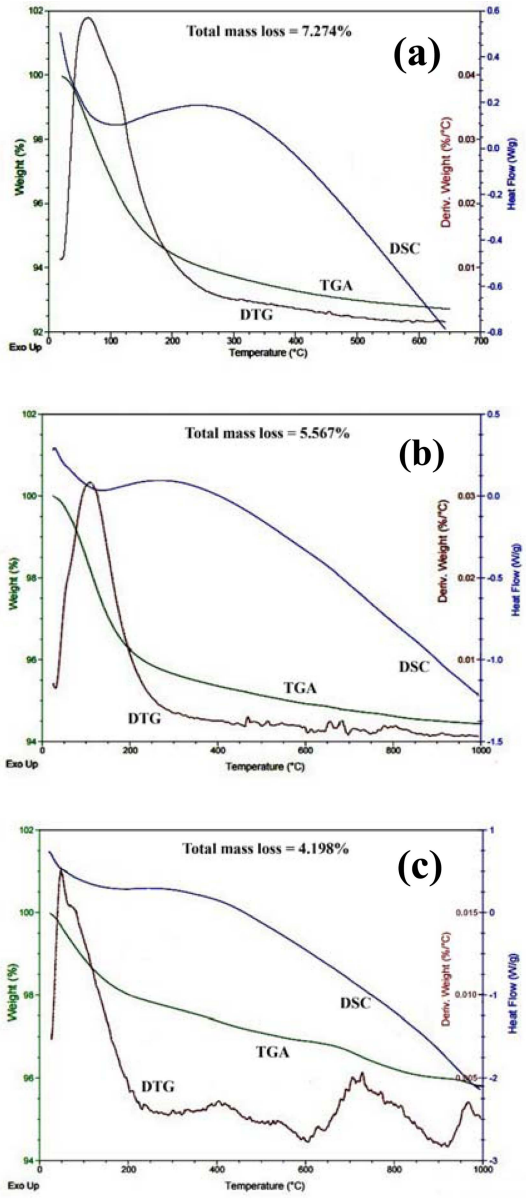


Fig. 9. Thermal properties measured by TGA-DSC and DTG of five-phase bioactive glasses; (a) 70S/10Fe, (b) 60S/20Fe, (c) 50S/30Fe.

reduction of total mass loss from 7.27% to 4.20%. Up to around 200 ºC, the first mass loss corresponding to a broad endothermic peak in a DSC curve is predominantly due to the removal of humidity or physically adsorbed waters trapped inside of the glass matrix [16]. Since these adsorbed waters are commonly trapped inside the glass structure [17], it follows that the reduction in SiO_2 composition results in a smaller amount trapped water. The DTG plot indicates the greatest rate of weight loss at varying temperatures which are 70, 109 and 48 ºC for samples 70S/10Fe, 60S/20Fe and 50S/30Fe, respectively.

The second mass loss over 200 ºC involves the structural densification and the crystallization. TGA curves exhibit the gradual decrease with only about 2%

mass loss. The rise in Fe proportions in these bioactive glasses slightly increases the second mass loss with 1.7, 1.8 and 2.2%, respectively for 10, 20 and 30% mol Fe. No DSC peak can be observed indicating the stability of these five-phase bioactive glasses in this temperature range. In the case of sample 60S/20Fe, the weak DTG peaks attributed to the densification and crystallization of glass structure locate around 470-510, 660-680, and 790-810 °C. For sample 50S/30Fe, the strong DTG peaks correspond to the greatest rate of weight loss at 403, 727, and 965 °C. Again, the peaks at 403 and 727 °C correspond to the densification. The peak at 965 °C can be assigned to the formation of crystalline structure since an exothermic differential thermal analysis (DTA) peak at around 960 °C was previously ascribed to the glass crystallization [18].

Conclusions

Sol-gel derived SiO_2-CaO-P_2O_5 retained bioactive glass chemical characteristics after incorporating Na_2O and γ-Fe_2O_3 phases as suggested by EDS and FTIR. However, their 3DOM scaffolds were distorted by both additives and the skeleton walls had larger variations in size and shape in the case of four- and five-phase bioactive glasses. It can be concluded that the sol can completely fill interstitial holes of the template in the case of three-phase SiO_2-CaO-P_2O_5 whereas the phase additions to four and five phases led to the spherical surface coating by the sol. In additions, the strong interactions of precursors in four- and five-phase bioactive glass affect the structural-phase separation and the 3DOM scaffolds are partially interrupted by microspheres formed at the external surface. Nevertheless, the five-phase bioactive glasses are rather thermally stable up to 1000 °C with only moderate first mass loss associated to the removal of physically adsorbed water and the second mass loss corresponding to the densification and the crystallization.

Acknowledgments

This work is financially supported by Walailak University, Shell Centennial Education Fund, Shell Companies in Thailand and Higher Education Research Promotion (HERP) of Thailand.

References

1. J.R. Jones, Acta Biomater. 9 (2013) 4457-4486.
2. Q.Z. Chen, Y. Li, L.Y. Jin, J.M.W. Quinn, and P.A. Komesaroff, Acta Biomater. 6 (2010) 4143-4153.
3. A. Lucas-Girot, F.Z. Mezahi, M. Mami, H. Oudadesse, A. Harabi, and M.L. Floch, J. Non-Cryst. Solids 357 (2011) 3322-3327.
4. E. Gentleman, Y.C. Fredholm, G. Jell, N. Lotfibakhshaiesh, M.D. O'Donnell, R.G. Hill, and M.M. Stevens, Biomaterials 31 (2010) 3949-3956.
5. M.E. Santocildes-Romero, A. Crawford, P.V. Hatton, R.L. Goodchild, I.M. Reaney, and C.A. Miller, J. Tissue Eng. Regen. Med. 9 (2015) 619-631.
6. R.J. Kavitha, B. Subha, S. Shanmugam, and K. Ravichandran, Int. J. Innov. Res. Sci. Eng. 1 (2014) 2347-3207.
7. M. Zhu, J. Zhang, Y. Zhou, Y. Liu, X. He, C. Tao, and Y. Zhu, J. Chem. 2013 (2013) 893479.
8. R.K. Singh, A. Srinivasan, and G.P. Kothiyal, J. Mater. Sci.: Mater. Med. 20 (2009) S147-S151.
9. C. Wu, W. Fan, Y. Zhu, M. Gelinsky, J. Chang, G. Cuniberti, V. Albrecht, T. Friis, and Y. Xiao, Acta Biomater. 7 (2011) 3563-3572.
10. T. Charoensuk, W. Limphirat, C. Sirisathitkul, P. Jantaratana, W. Tangwatanakul, and U. Boonyang, Nanomater. Nanotechnol. 5 (2015) 34.
11. M. Farahmandjou, and N. Golabiyan, J Ceram. Proc. Res. 16 (2015) 237-240.
12. J. Ma, C.Z. Chen, D.G. Wang, and J.Z. Shi, Mater. Sci. Eng. C 30 (2010) 886-890.
13. A. Stein, F. Li, and N.R. Denny, Chem. Mater. 20 (2008) 649-666.
14. D. Wang, H. Lin, J. Jiang, X. Han, G. Wei, X. Wu, Y. Jin, and F. Qu, Sci. Technol. Adv. Mater. 14 (2013) 025004.
15. S.G. Rudisill, S. Shaker, D. Terzic, R.G.L Maire, B.L. Su, and A. Stein, Inorg. Chem. 54 (2015) 993-1002.
16. A.C. Jayalekshmi, S.P. Victor, and C.P. Sharma, Colloids Surf. B Biointerfaces. 101 (2013) 196-204.
17. T. Charoensuk, C. Sirisathitkul, and U. Boonyang, Rev. Rom. Mater. 43 (2013) 320-325.
18. L.M. Mukundan, R. Nirmal, D. Vaikkath, and P.D. Nair, Biomatter. 3 (2013) e24288.

View publication stats